ACS Catalysis

Research Article

Cite This: ACS Catal. 2019, 9, 1595−1604

pubs.acs.org/acscatalysis

Anionic Single-Atom Catalysts for CO Oxidation: Support-Independent Activity at Low Temperatures

Thomas Kropp,*[,†] Zhuole Lu,[‡] Zhao Li,[‡] Ya-Huei Cathy Chin,[‡] and Manos Mavrikakis*[,†]

[†]Department of Chemical and Biological Engineering, University of Wisconsin—Madison, 1415 Engineering Drive, Madison, Wisconsin 53706-1607, United States

[‡]Department of Chemical Engineering and Applied Chemistry, University of Toronto, 200 College Street, Toronto, Ontario M5S 3E5, Canada

Supporting Information

ABSTRACT: We study 14 atomically dispersed transition metals on halite-type oxides (MeO, Me = Fe, Mg, Mn, and Ni) using periodic density functional theory calculations and probe structure and activity toward CO oxidation for a subset of these systems experimentally. Pd and Pt can form stable negatively charged species upon binding to oxygen vacancies; the magnitude of the metal atom binding energy depends on the O vacancy formation energies of the supporting metal oxide and the lattice match between transition metal and support. The resulting oxide-supported single-atom systems catalyze CO oxidation by molecularly adsorbed O_2 with intrinsic barriers as low as 36 kJ/mol for Pt/MnO_x(001). This high activity stems from the single sites' ability to stabilize surface superoxide species. Furthermore, intrinsic barriers were found to depend primarily on the identity of the transition metal and to be nearly independent of the support identity. However, O_2 may heal the oxygen vacancy, which leads to catalyst deactivation. Catalyst deactivation by oxygen can be suppressed by using a more reducible support such as FeO(001) or MnO(001).

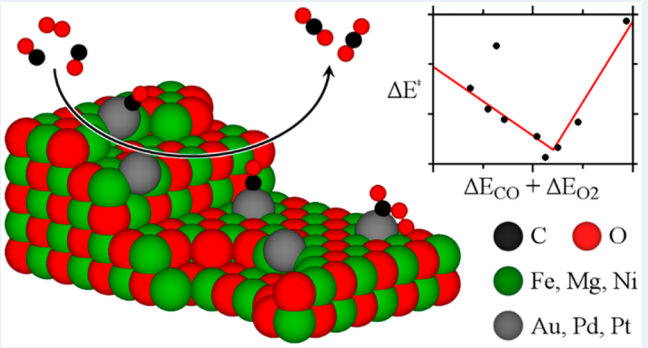

KEYWORDS: *atomic dispersion, density functional theory, CO oxidation, oxides, single-atom catalyst*

1. INTRODUCTION

For catalytic applications, transition metals are typically dispersed on the surface of a less expensive support, as this decreases the percentage of inaccessible bulk metal atoms. The catalytic activity of these supported metal particles generally depends on their size.[1−3] Atomically dispersed catalysts, or single-atom catalysts, are particularly desirable systems. Because of their uniform active sites, single-atom catalysts provide superior selectivity.[4] These advantageous properties are responsible for an increase in research interest in this topic in recent years (e.g., refs 5 and 6).

Among other support materials, metal oxides such as Al_2O_3,[7−11] CeO_2,[12−14] CuO,[15] Fe_2O_3,[16−19] Fe_3O_4,[20] MnO_2,[21] and MgO[22−24] have been used for the synthesis of single-atom catalysts. For most of these systems, the transition metal atoms bind to O ions, though Abbet et al. were able to stabilize single Pd atoms inside the O vacancies of MgO.[22,23] Upon removing a neutral O atom from MgO, the two excess electrons localize in the now vacant O lattice position, forming an F^0 center. Pd atoms binding inside F^0 centers of MgO were found to enable CO oxidation at temperatures below 260 K, but the Pd atoms agglomerate upon CO_2 formation, leading to catalyst deactivation.[23]

Small Au_n clusters (n < 20) supported on O-defective MgO catalyze the oxidation of CO at similar temperatures (240 K).[25] This high activity is the result of an electron transfer from the F^0 center to the Au d orbitals.[26] Using density functional theory (DFT), Li and co-workers[27] studied CO oxidation catalyzed by late transition metal atoms supported in F^0 centers of MgO. They report CO oxidation barriers as low as 25 kJ/mol (Ag/MgO_x), but they do not address the stability of their single-atom catalysts.

Using periodic DFT calculations, we study CO oxidation on transition-metal atoms supported on the (001) surface of MeO (Me = Fe, Mg, Mn, and Ni). While previous studies[28−31] have highlighted the role of surface OH species for low-temperature CO oxidation, this study focuses on O_2 activation at low temperatures. We find that Pd and Pt can form thermodynamically favorable single sites inside O vacancies; the magnitude of the metal atom binding energy depends on the oxygen vacancy formation energy and the lattice constant of the supporting metal oxide. On the basis of these predictions, three Pt/MeO catalysts (Me = Fe, Mg, and Mn) were prepared

Received: August 17, 2018
Revised: January 4, 2019
Published: January 25, 2019

DOI: 10.1021/acscatal.8b03298
ACS Catal. 2019, 9, 1595−1604

experimentally. Pt atoms inside O vacancies were identified on the basis of their characteristic CO stretching mode at 1997 cm^{-1} in the infrared spectrum. Importantly, single-atom catalysts supported on metal oxides with high O vacancy formation energies such as MgO are not stable under CO oxidation conditions, which is in agreement with previous experimental work.[23] Therefore, oxides with moderate vacancy formation energies such as FeO or MnO are predicted to be more suitable support materials for atomically dispersed Pd and Pt catalysts. For Pt atoms supported on MgO, MnO, and FeO, sintering was observed experimentally at temperatures around 336, 348, and 366 K, respectively, which is in good agreement with the predictions from DFT.

2. METHODS

2.1. Computational. Calculations were performed using the projector augmented wave (PAW) method[32,33] as implemented in the Vienna *ab initio* simulation package (VASP).[34,35] Exchange−correlation energies were obtained using the functional by Perdew, Burke, and Ernzerhof (PBE).[36] Onsite Coulomb correlation of occupied d orbitals was corrected with the DFT+U approach[37,38] using effective Hubbard-type parameters of 4.0 eV (Fe and Mn) and 6.3 eV (Ni); these values are derived in refs 39−41, respectively. The implementation of DFT+U follows Dudarev et al.[42] A plane wave cutoff of 600 eV was used. Structure optimizations were performed until total energies were converged to 10^{-6} eV, and forces acting on the relaxed ions were below 0.02 eV/Å. Transition state structures were obtained using the improved dimer method.[43,44] VESTA was used to visualize structures.[45]

Vibrational frequencies were obtained by diagonalizing a partial, mass-weighted matrix of second derivatives with respect to the three Cartesian degrees of freedom of each atom. This "Hessian" matrix was obtained by finite differences of the gradients with displacements of ±0.015 Å (central differences). Structures were proven to be minima by the absence of imaginary frequencies. For transition-state structures, one imaginary frequency was obtained.

The $c(2 \times 2)$ surface unit cells were obtained by cutting the bulk oxides in (001) orientation. Optimized lattice constants (Table 1) are in good agreement with the values reported in refs 40, 41, and 46; compared with experimental lattice constants,[47] they are overestimated by 1−2%. The slab models consist of five atomic layers, of which the bottom two layers are frozen to simulate the bulk. Increasing the number of atomic layers changes the surface energies by less than 0.01 J/m^2. The vacuum layer was set to 1 nm. The Brillouin zone was sampled at $3 \times 3 \times 1$ k points. Increasing the number of k points changes total energies by less than 1 meV. Structural parameters for the bulk transition metals considered in this work are given in Table S1. For metals, the Brillouin zone was sampled at $20 \times 20 \times 20$ k points.

Table 1. Local Magnetic Moments m [μ_B] of Cations, Lattice Constants a [Å], Surface Energies γ [J/m^2], and Oxygen Vacancy Formation Energies ΔE_{def} [kJ/mol] from eq 1 for the (001) Surfaces of the Oxide Supports Considered in This Work

	m	$a_{PBE(+U)}$	a_{exp}	γ	ΔE_{def}
FeO	3.7, 3.7[a]	4.39	4.29[e]	0.62	301
MnO	4.6, 4.6[b]	4.52, 4.48[b]	4.44[e]	0.63	424
NiO	1.8, 1.7[c]	4.24, 4.20[c]	4.19[e]	0.83	437
MgO	0	4.26, 4.26[d]	4.20[e]	0.89	582

[a]ref 39. [b]ref 40. [c]ref 41. [d]ref 46. [e]ref 47.

O-defective surfaces were obtained by removing a surface O atom ($\theta = 1/8$). Oxygen vacancy formation energies ΔE_{def} are calculated using eq 1 and increase in the order FeO < MnO < NiO < MgO as shown in Table 1.

$$\Delta E_{def} = E(Me_{40}O_{40}) - E(Me_{40}O_{39}) - 1/2E(O_2) \quad (1)$$

2.2. Experimental Section. *2.2.1. Catalyst Synthesis.* Pt/MeO_x-SiO_2 catalysts (0.1 wt % Pt and 10 wt % Me, Me = Mg, Mn, Fe) were prepared by wet impregnation method. The precursor, $Mg(NO_3)_2 \cdot 6H_2O$ (99.0%; Sigma-Aldrich), $Mn(NO_3)_2 \cdot 4H_2O$ (>97.0%; Sigma-Aldrich), or $Fe(NO_3)_3 \cdot 9H_2O$ (99.999%; Sigma-Aldrich), was dissolved in 3 cm^3 doubly deionized water (>18 MΩ cm). The solution was added dropwise to a 7 cm^3 suspension containing 3 g of SiO_2 under constant stirring at ambient temperature. The suspension was stirred for another 12 h at ambient temperature and then dried at 393 K in the oven for 12 h. The solid support was heated to 823 K at 2 K/min for 4 h in flowing dry air (Linde, GR 0.1).

The "as-prepared catalyst" was synthesized as follows: the Pt precursor ($H_2PtCl_6 \cdot 6H_2O$, Sigma-Aldrich, 99.9% trace metal bases) was dissolved in 1 cm^3 deionized water; this solution was added dropwise to 4 cm^3 of a liquid suspension containing the support powders (1 g) and doubly deionized water (4 cm^3, > 18 MΩ cm) at ambient temperature. The suspension was stirred continuously for 12 h and then dried at 353 K for 12 h before heating at 2 K/min to 673 K for 2 h under flowing dried air (Linde, GR 0.1).

2.2.2. CO and H_2 Uptake. CO chemisorption studies were carried out using a customized volumetric adsorption−desorption apparatus at 303 K. For each experiment, 300 mg of catalyst powder were loaded into a quartz sample holder. The catalyst was reduced with 10% H_2 (Linde, 99.999%) in He (Linde, 99.99%) at a flow rate of 50 mL/min while the temperature was increased to 473 K. Then, the reactor was evacuated under dynamic vacuum (10^{-5} Pa) at 473 K for at least 12 h and cooled to 303 K. After this pretreatment, 5% CO (Linde, certified standard) was introduced to the sample in small increments (5 to 20 μmol per dose) until the CO partial pressure inside the reactor, which was measured by a pressure transducer (MKS, 120AA Baratron), increased to 0.4 kPa. For H_2 uptake tests, the same procedure was used, except the CO/He mixture was replaced with H_2 (Linde, 99.999%). The chemisorption experiments were repeated after the temperature-programmed CO oxidation experiments to study Pt sintering during the reaction.

2.2.3. Infrared Measurements. In situ Fourier-transform infrared spectroscopy (FTIR) was carried out using a Bruker Vertex 70 equipped with a mercury cadmium telluride (MCT) detector in transmission mode using an environmental cell equipped with KBr windows and a K-type thermocouple, which is mounted onto the sample holder and connected to a temperature controller. Prior to each experiment, the catalyst powder was pelletized into a thin disk (~1.3 cm diameter and ~25 mg/cm^2 surface density) and placed in the sample holder. The inlet gases were controlled by mass flow meters (Brooks, SLA5850). Infrared spectra were taken between 500 and 4000 cm^{-1} at 296 K with a resolution of 0.40 cm^{-1}, averaging over 16 scans at 0.40 cm^{-1} intervals.

For each experiment, the catalyst disk was first exposed to 10% H_2 (Linde, 99.999%) in He (Linde, 99.99%) at a flow rate

DOI: 10.1021/acscatal.8b03298
ACS Catal. 2019, 9, 1595−1604

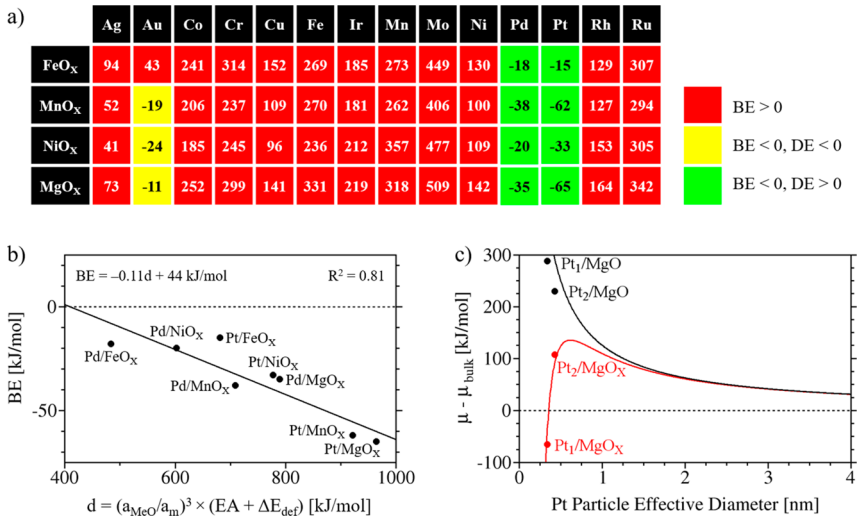

Figure 1. (a) Binding energies (BE) in kJ/mol for transition metal atoms in O vacancies of MeO(001). Positive values are indicated by a red entry. A yellow box indicates exothermic metal dimer formation energies (DE), while green boxes indicate endothermic dimer formation; DE is not given in the respective boxes. Binding energies on the pristine metal oxide surfaces can be found in Table S2. (b) Binding energies for Pd and Pt atoms in O vacancies of MeO(001) are shown as a function of the lattice constants of metal (a_m) and metal oxide (a_{MeO}), the electron affinity of the metal (EA), and the O vacancy formation energy of the support (ΔE_{def}). (c) Binding energies for Pt atoms and dimers on pristine and O-defective MgO(001), that is, MgO and MgO_x, are compared to the chemical potential of Pt particles supported on MgO from eq 4 (black) and eq 5 (red), respectively.

Table 2. Bader Charges Q of the Transition Metal Atom, Binding Energies (BE) for First CO and O_2 Adsorbing (cf. Figure 2), and CO Oxidation Barriers via TS1 ($\Delta E^{\ddagger}$)[a]

		binding energies				barrier decomposition				
	Q	BE_{CO+O_2}	BE_{CO}	BE_{O_2}	ΔE_{int}	$\Delta E^{\ddagger}$	ΔE_{CO}	ΔE_{O_2}	$\Delta E^{\ddagger}_{int}$	ΔE_{relax}
Au/FeO_x[b]	−0.71	−205	−86	−167	48					−83
Au/MnO_x	−0.78	−168	−32	−149	13	**31**	2	60	−31	−139
Au/NiO_x	−0.63	−141	−25	−114	−2	**36**	1	60	−25	−161
Au/MgO_x	−0.75	−203	−46	−182	26	**33**	4	60	−31	−251
Pt/FeO_x	−0.97	−171	−115	−65	9	**45**	16	47	−18	11
Pt/MnO_x	−1.12	−174	−103	−54	−18	**36**	7	54	−25	−45
Pt/NiO_x	−0.81	−150	−119	−19	−12	**39**	23	34	−18	−82
Pt/MgO_x	−1.65	−126	−109	−42	25	**38**	15	54	−31	−220
Pd/FeO_x	−0.78	−147	−85	−43	−20	**45**	6	41	−2	−36
Pd/MnO_x	−0.94	−162	−82	−58	−22	**42**	7	45	−10	−130
Pd/NiO_x	−0.65	−148	−93	−37	−18	**53**	18	36	−1	−161
Pd/MgO_x	−1.53	−144	−88	−40	−16	**64**	11	67	−14	−292

[a] $\Delta E_{int} = BE_{CO+O_2} - BE_{CO} - BE_{O_2}$ is the interaction energy of CO and O_2. ΔE_{CO}, ΔE_{O_2}, and $\Delta E^{\ddagger}_{int}$ are obtained via barrier decomposition, and ΔE_{relax} is the relaxation energy of the MeO species (cf. Figure 4). All energies are given in kJ/mol. [b] Not considered for CO oxidation due to weak binding of Au on O-defective FeO (cf. Figure 1).

of 50 mL/min. The sample was heated to 473 K at 0.5 K/min and sequentially held at 473 K for 0.5 h. After that, the disk was cooled to 296 K and exposed to 2% CO (Linde, certified standard) in He (Linde, 99.99%) for 10 min at a flow rate of 50 mL/min, after which the absorbance features remained unchanged with time. The cell was then purged with He (Linde, 99.99%) at a flow rate of 50 mL/min for 0.5 h to remove gaseous CO before measuring the absorbance spectrum. To study the oxidation of preadsorbed CO, 10% O_2 (Linde, 99.99%) in He (Linde, 99.99%) was introduced into the cell at a flow rate of 50 mL/min for 30 min at 296 K before measuring the absorbance spectrum.

2.2.4. Evaluation of CO Oxidation Rates. CO oxidation experiments were carried out with a U-shaped quartz reactor connected to a gas chromatograph (SRI-GC) equipped with a methanizer and FID detector. Prior to the reactivity testing, the samples were pelletized and sieved to 80−120 mesh. Catalysts (50 mg) were loaded into the reactor and pretreated with 10% H_2 (Linde, 99.999%) in He (Linde, 99.99%) at a flow rate of 50 mL/min at 473 K for 0.5 h before they were cooled to ambient temperature under flowing He.

The temperature-programmed reaction was carried out between 303 and 473 K with a heating rate of 0.5 K/min. The feed gas, which contains 0.4 kPa CO (Linde, certified standard) and 10 kPa O_2 (Linde, 99.99%) with balance He (Linde, 99.99%), was introduced to the reactor at 100 cm^3/min. The chemical composition of the effluent stream from the reactor was analyzed with a gas chromatograph at sampling intervals of 3 min. Turnover frequencies (TOF) refer to the number of CO molecules converted via eq 2 per second and are normalized by the total number of Pt atoms.

DOI: 10.1021/acscatal.8b03298
ACS Catal. 2019, 9, 1595−1604

$$CO + 1/2O_2 \rightarrow CO_2 \quad (2)$$

3. RESULTS AND DISCUSSION

3.1. Insights into Metal−Support Interactions from DFT. We find that transition metal atoms (m) bind preferably atop O ions on the pristine oxide surfaces. On the reducible oxides (i.e., FeO, MnO, and NiO), the O−m axis is slightly tilted toward a neighboring cation. This has been previously reported by Janik and co-workers,[48] who found that the binding energies (BE) were correlated with, among other factors, the electron affinity (EA) of the metal and the O vacancy formation energy of the supporting oxide. However, binding energies calculated relative to bulk metal atoms (m_{bulk} in eq 3) are positive at $\theta = 1/8$(Table S2), which indicates that the formation of metallic particles is thermodynamically favored over atomic dispersion.

$$BE = E(m_1/Me_{40}O_{40}) - E(Me_{40}O_{40}) - E(m_{bulk}) \quad (3)$$

Calculated binding energies for metal atoms inside O vacancies are less positive for all transition metals except Mn, which has a negative electron affinity.[49] Transition metals with low electron affinities (Cr, Fe, and Mo) bind only to O vacancies with high defect formation energies. However, only the binding energies for Au, Pd, and Pt inside O vacancies are negative (Figure 1a). Based on the difference between the binding energies on pristine and O-defective oxide surfaces (Table S2), it requires more than 100 kJ/mol to move a Pd or Pt atom from an O vacancy onto a terrace site.

The strong binding of Au, Pd, and Pt atoms to O vacancies of MeO(001) is the result of a charge transfer from the defect states into the energetically lower metal states, which has been previously reported for MgO-supported transition metals.[50] On MgO, this leads to Bader charges of −0.75 (Au), −1.53 (Pd), and −1.65 (Pt) for the transition metal atoms (Table 2). For the reducible oxide supports (FeO, MnO, and NiO), lower Bader charges were obtained for Pd and Pt, indicating a less pronounced charge transfer compared to the nonreducible MgO support.

The energy gain of the electron transfer depends on the energy difference between the corresponding orbitals. Thus, O vacancies with high-energy defect states, i.e. high vacancy formation energies ΔE_{def}, bind transition metals more strongly. This is qualitatively different from the adsorption on pristine oxide surfaces, where binding energies of metal atoms are more exothermic on reducible oxides.[48] The energy level of the acceptor states, on the other hand, depends on the electron affinity EA of the transition metal. While binding energies of metal atoms in the O vacancies of MeO(001) were found to correlate with both properties, an additional structural component is needed to reproduce binding energy trends. The descriptor $d = (a_{MeO}/a_m)^3 \times (EA + \Delta E_{def})$, where a_m and a_{MeO} are the lattice constants of metal and metal oxide, respectively, correctly predicts binding energy trends following $FeO_x < NiO_x < MnO_x \approx MgO_x$ with a mean absolute error of 7 kJ/mol; the fit for Pd and Pt is shown in Figure 1b, and the underlying data is compiled in Table S3. While the descriptor utilizes the lattice constant of the transition metal (a_m), it refers to the binding of a negatively charged metal species in the O vacancy. The charge transferred to the metal atom upon adsorption leads to an increase in size, which is why an a_{MeO}/a_m ratio greater than 1 actually enhances the binding interaction between MeO_x and m. The descriptor also predicts that Pt does not form stable single-atom catalysts inside O vacancies of $CeO_2(111)$, a support material with a lower vacancy formation energy (199 kJ/mol in ref 51) than any oxide considered in this work. This is in good agreement with results by Fabris and co-workers.[13]

While these calculations demonstrate that atomic dispersion of Au, Pd, and Pt is more stable than the formation of extended particles on the four oxide surfaces (with the exception of Au/FeO_x; see Figure 1a), one has yet to show that atomic dispersion is also more stable than cluster growth at the O vacancies. For Pd and Pt dimers at O vacancies, binding energies per metal atom are significantly less exothermic than the values for single atoms, as no additional charge transfer occurs. While larger clusters might be more stable than dimers, this indicates that particle formation is hindered by large barriers. Thus, atomic dispersion is favorable at low coverage, which is in good agreement with experimental findings in ref 23. For Au dimers, the binding energy per metal atom is similar to the value for the first atom. This would lead to a statistical cluster size distribution even at low coverage, which is in good agreement with previous DFT results in ref 52.

Interestingly, DFT binding energies for single atoms of Pd (218 kJ/mol) and Pt (288 kJ/mol) on pristine MgO(001) are similar to values extrapolated from experimental data by Hemmingson and Campbell,[53] that is, 279 kJ/mol for Pd and 323 kJ/mol for Pt. They approximate the chemical potential of metal atoms in supported hemispherical nanoparticles using eq 4, where γ is the surface energy of the metal nanoparticle, E_{adh} is the adhesion energy between particle and support, V_m is the molar volume of the transition metal, and D is the effective diameter of the particle.

$$\mu - \mu_{bulk} = (3\gamma - E_{adh})2V_m/D \quad (4)$$

The chemical potential for Pt atoms in hemispherical nanoparticles supported on MgO(001) is plotted in Figure 1c (black line) using experimental values for V_m (9.09×10^{-7} m^3/mol), γ (2.52 J/m^2), and E_{adh} (1.51 J/m^2) from ref 54. The effective diameter for the Pt_n particles was calculated using $D = \sqrt[3]{16n}\,r_a$, where r_a is the atomic radius of Pt (135 pm). This equation is derived by equating the volume of n Pt atoms and the volume of a hemisphere with diameter D. Binding energies obtained in this work using PBE (black circles in Figure 1c) are close to the values predicted by eq 4.

However, binding energies for Pt clusters inside O vacancies (red circles in Figure 1c) are poorly approximated by eq 4. Qualitative agreement can be achieved by adding an additional term C/D^3 (eq 5; red line in Figure 1c for $C = 16$ kJ m^3/mol; value obtained by fitting to DFT data), which represents a stronger binding for the first Pt atom. Since the number of metal atoms scales with D^3, this stabilizing interaction has to scale with $1/D^3$. This modification does not significantly affect the chemical potential for nanoparticles with $D > 1$ nm (more than 25 atoms), but it introduces a local or global minimum corresponding to atomic dispersion depending on the value of C.

$$\mu - \mu_{bulk} = (3\gamma - E_{adh})2V_m/D - C/D^3 \quad (5)$$

On the basis of these DFT results, we conclude that Pd and Pt can form stable single-atom catalysts inside the O vacancies of metal oxides. Binding energies were found to depend on O vacancy formation energies and the lattice match between transition metal and support. Because of their higher electron

DOI: 10.1021/acscatal.8b03298
ACS Catal. 2019, 9, 1595−1604

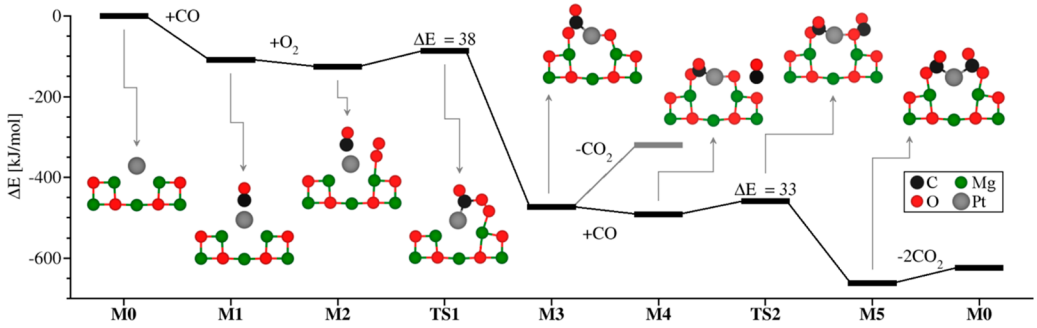

Figure 2. Energy profile for the CO oxidation on Pt/MgO_x with cross-sectional views on reaction intermediates. The following color code is used throughout this work: C (black), Mg (green), O (red), and Pt (gray). The axis label M indicates a minimum, whereas TS represents a transition state along the reaction coordinate.

affinity, Pt-based catalysts are predicted to be more stable than the Pd/MgO_x catalyst reported by Landman and co-workers.[23]

3.2. CO Oxidation Activity: Insights from DFT. On the basis of DFT calculations, Li and co-workers[27] concluded that the CO oxidation on metal atoms supported on O-defective MgO(001), denoted here as m/MgO_x(001), follows a Langmuir−Hinshelwood mechanism. In this work, the same mechanism is adopted, but reaction energies and barrier heights were found to be different, because Li and co-workers[27] did not allow for surface relaxation. Other oxidation pathways with even lower barriers may be feasible on the reducible oxide supports. Thus, barriers reported in this section represent an upper bound for the overall CO oxidation barriers. However, this upper bound already indicates low-temperature oxidation activity. In this section, CO oxidation on Pt/MgO_x(001) will be discussed in detail, but similar intermediates were obtained for the other single-atom catalysts considered in this work.

CO and O_2 adsorb on the Pt atom of **M0** (Figure 2) with individual adsorption energies of −113 and −43 kJ/mol, respectively. Because of backbonding, the C−O bond in **M1** is elongated by 2% upon adsorption, leading to a redshift of the calculated CO stretching mode (1994 cm^{-1} for **M1** compared to 2126 cm^{-1} for gas phase CO, which is 18 cm^{-1} lower than the experimental value of 2144 cm^{-1} in ref 55). A similarly red-shifted CO stretching mode (2005 cm^{-1}) was experimentally observed for CO on Pd/MgO_x(001).[23] Upon O_2 adsorption, the O−O bond is elongated by 4%, which corresponds to the formation of a superoxide species. The coadsorption energy (−131 kJ/mol in **M2**) includes a destabilizing interaction of ΔE_{int} = 25 kJ/mol, as both adsorbates compete for electron density from Pt. While the preferred adsorption mode of CO is not affected by varying the support, O_2 was found to preferably adsorb on a bridging site between two surface cations on the reducible oxide supports.

The oxidation barrier via **TS1** (cf. Figure 2) amounts to 38 kJ/mol, which is significantly lower than the value reported in ref 27 (133 kJ/mol). Li and co-workers[27] used the same density functional (PBE) and a comparable unit cell size, i.e $p(3 \times 3)$ compared to $c(2 \times 2)$ in this work. However, they did not allow for surface relaxation, which stabilizes intermediates and transition state structures significantly. Along the imaginary mode of **TS1** (595 cm^{-1}), the O−O bond breaks, and an O atom is transferred to CO.

CO_2 desorption from the resulting PtO cluster (**M3**) is 153 kJ/mol endothermic (gray path starting with **M3** in Figure 2). Alternatively, a second CO molecule may adsorb atop a Mg^{2+} ion in the vicinity of the active site with an adsorption energy of −18 kJ/mol (**M4**). Adsorption atop the Pt atom is less favorable in the presence of adsorbed CO_2 and atomic O.

The oxidation barrier via **TS2** amounts to 33 kJ/mol, which is lower than the barrier for the first oxidation step (38 kJ/mol). Along the imaginary mode of **TS2** (438 cm^{-1}) the CO molecule moves toward the O atom, and the Pt−O bond is elongated. Starting with **M5**, CO_2 desorption is only mildly endothermic (19 kJ/mol for each CO_2 molecule). Compared to the PtO species **M3**, which binds CO_2 more strongly (153 kJ/mol), the Pt atom of **M5** is 15 pm closer to the MgO(001) surface (see side views in Figure 2). As the Pt species binds more strongly to the Mg^{2+} cations, it binds CO_2 less strongly, facilitating the desorption step after the formation of the second CO_2 molecule.

Calculated adsorption energies and barrier heights for single-atom catalysts studied in this work are compiled in Table 2. On Pt/MeO_x(001), *intrinsic* barriers amount to 45 kJ/mol (Pt/FeO_x), 36 kJ/mol (Pt/MnO_x), and 38 kJ/mol (Pt/MgO_x). Our experimentally determined *apparent* barriers (Figure S2) are slightly lower than the calculated intrinsic barriers, that is, 15 kJ/mol (Pt/FeO_x), 28 kJ/mol (Pt/MnO_x), and 30 kJ/mol (Pt/MgO_x). This is likely due to the weak binding energies for O_2 in the presence of a preadsorbed CO molecule, which is why the experimental barrier refers to the transition from **M1** to **M3** (Figure 2). The most exothermic O_2 binding energy was calculated for Pt/FeO_x, which would explain why the apparent oxidation barrier is lower on the FeO_x support.

On Pd/MgO_x(001), the intrinsic CO oxidation barrier amounts to 64 kJ/mol. Using the Redhead equation,[56] this barrier would correspond to a CO_2 desorption peak at 250 K in temperature-programmed reaction experiments, which is close to the observed peak at 260 K.[23]

On each metal oxide support, intrinsic oxidation barriers increase in the order Au < Pt < Pd. While Bader charges Q on the metal atoms and adsorption energies of CO and O_2 depend on the nature of the support, CO oxidation barriers are surprisingly similar. On Au and Pt atoms, CO oxidation barriers are within 5 and 9 kJ/mol, respectively, regardless of the support. For Pd atoms, a larger spread (22 kJ/mol) was obtained. However, even this larger spread is still within the accuracy of our DFT approach. Furthermore, each system is predicted to show CO oxidation activity at low temperatures due to the small intrinsic barriers.

To gain a more detailed understanding of the factors contributing to the oxidation barrier $\Delta E^{\ddagger}$, the barrier is decomposed into the following terms: (i) ΔE_{CO} is the energy

DOI: 10.1021/acscatal.8b03298
ACS Catal. 2019, 9, 1595−1604

required to move an isolated CO molecule from its most stable adsorption site to its position in **TS1**; (ii) ΔE_{O_2} is the energy required to move an isolated O_2 molecule from its most stable adsorption site to its position in **TS1**; and (iii) $\Delta E_{int}^{\ddagger} = \Delta E^{\ddagger} - \Delta E_{CO} - \Delta E_{O_2}$ is the interaction energy between CO and O_2 in **TS1**. The energy contributions are compiled in Table 2 and visualized in Figure S1.

ΔE_{CO} increases as the binding of CO becomes more exothermic. Furthermore, ΔE_{CO} increases with the Bader charge of the transition metal atom, which depends on the reducibility of the support as discussed in the previous section. For Au clusters, this correlation between charge and CO binding energies has been previously demonstrated using DFT.[57] On the other hand, ΔE_{O_2} is lower for reducible supports. Since O_2 binds at the metal−support interface, charge transfer into the O_2 π^* orbitals (i.e., superoxide formation) can originate from the metal atom or the support, lowering the barrier for O_2 dissociation. While CO and O_2 compete for electron density from the metal atom, only O_2 can withdraw electron density from the d bands of the support. This leads to a more pronounced charge transfer into the O_2 π^* orbitals for reducible supports, as indicated by longer O−O bonds for molecularly adsorbed O_2. Because of this negative correlation between ΔE_{CO} and ΔE_{O_2} (Figure 3), CO oxidation

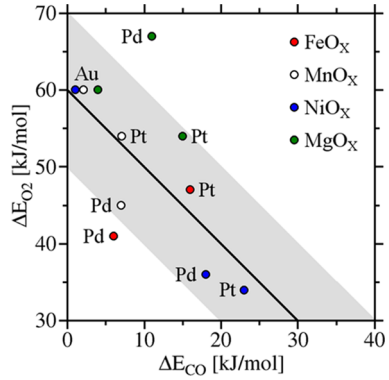

Figure 3. Inverse correlation between ΔE_{CO} and ΔE_{O_2} (cf. Table 2). The black line refers to the linear fit $\Delta E_{O_2} = 60$ kJ/mol $- \Delta E_{CO}$ ($R^2 = 0.41$), and the gray area indicates an uncertainty of ±10 kJ/mol. The color of the spheres indicates the support material: red (FeO_x), white (MnO_x), blue (NiO_x), and green (MgO_x).

barriers on a particular transition metal do not vary significantly for different supporting oxides. However, intrinsic oxidation barrier heights increase in the order Au < Pt < Pd for each support. This correlates with a decrease in the average interaction energy $\Delta E_{int}^{\ddagger}$ between CO and O_2 in the transition state (−28 kJ/mol for Au, −23 kJ/mol for Pt, and −7 kJ/mol for Pd).

3.3. Experimental Infrared Spectra and Chemisorption Studies. CO adsorption on bare MgO_x (Figure 4a) does not lead to detectable infrared features between 2200 and 1800 cm^{-1}; the peak at 1356 cm^{-1} is assigned to CO molecules inside O vacancies of MgO based on reference frequencies obtained using DFT (1347 cm^{-1}). DFT binding energies and harmonic frequencies that are discussed in this section have been compiled in Table S4. The total CO uptake amounts to 0.57 μmol/g_{cat}. As CO can bind to other vacancy-type defects (e.g., Schottky-type double vacancies) as well,[58] this should be

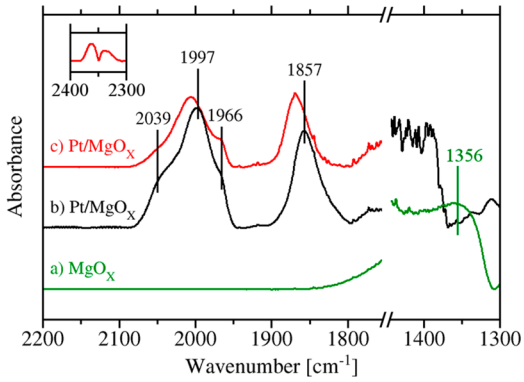

Figure 4. Infrared spectra of (a) MgO_x and (b) 0.1 Pt/MgO_x after exposure to 2 kPa CO and purging under flowing He at 296 K. (c) The CO-covered Pt/MgO_x sample was then exposed to 10% O_2 for 30 min (flow rate 50 mL/min) at 296 K. The inset shows C−O stretching features resulting from CO_2.

considered an upper limit for the O vacancy concentration. The infrared signal at 1356 cm^{-1} is notably absent for CO adsorbed on Pt/MgO_x (Figure 4b), which indicates that Pt binds to the O vacancies instead. This interpretation is further supported by a decrease in the amount of weakly adsorbed CO in the titration experiments (0.47 μmol/g_{cat}).

On Pt/MgO_x, additional infrared features are observed at 2039, 1997, 1966, and 1857 cm^{-1}. The peak at 1997 cm^{-1} is assigned to CO on Pt atoms inside O vacancies (1994 cm^{-1} from DFT), and the shoulder at 1966 cm^{-1} is assigned to the symmetric C−O stretching mode of two coadsorbed CO molecules on single Pt atoms inside O vacancies (1978 cm^{-1} from DFT); the antisymmetric C−O stretching mode (1935 cm^{-1} from DFT) is predicted to be nearly IR-inactive because of the small dipole change along the normal mode. However, the intensity of the peak at 1997 cm^{-1} is significantly higher, which indicates that single Pt atoms predominantly bind one CO molecule. The left-hand shoulder at 2039 cm^{-1} is assigned to CO atop metallic Pt atoms (2045 cm^{-1} for Pt(001) from DFT), and the peak at 1857 cm^{-1} is assigned to CO in a bridged configuration on Pt facets (1842 cm^{-1} for Pt(001) from DFT). For positively charged Pt species, significantly more blue-shifted CO stretching modes have been reported (e.g., 2118 cm^{-1} for Pt/Al_2O_3 and 2098 cm^{-1} for Pt/CeO_2 in refs 8 and 14, respectively), which indicates that no such species are present on the MgO_x support. Thus, our Pt/MgO_x catalyst contains a mix of O vacancy-supported single atoms and Pt clusters/particles.

To study the oxidation of preadsorbed CO, 10% O_2 in He was introduced into the cell at 296 K. The resulting infrared spectrum (Figure 4c) shows a decrease in the adsorption band intensity for CO adsorbed on atomically dispersed Pt (1997 cm^{-1}). Compared with CO, O_2 binds less strongly to Pt/MgO_x (−42 kJ/mol for O_2 and −109 kJ/mol for CO), so the loss in infrared intensity is likely a result of CO oxidation rather than displacement of CO by O_2 at this temperature. Furthermore, two additional infrared bands are observed at 2362 and 2339 cm^{-1} (inset in Figure 4), which are assigned to CO_2 product; based on DFT calculations, the C−O stretching mode for CO_2 on Pt_1/MgO_x is predicted to occur at 1818 cm^{-1}, which would overlap with the broad peak for bridged CO at 1857 cm^{-1}. The peak for CO in a bridging configuration at 1857 cm^{-1} is blue-shifted to 1868 cm^{-1} and decreases in intensity as well. This

DOI: 10.1021/acscatal.8b03298
ACS Catal. 2019, 9, 1595−1604

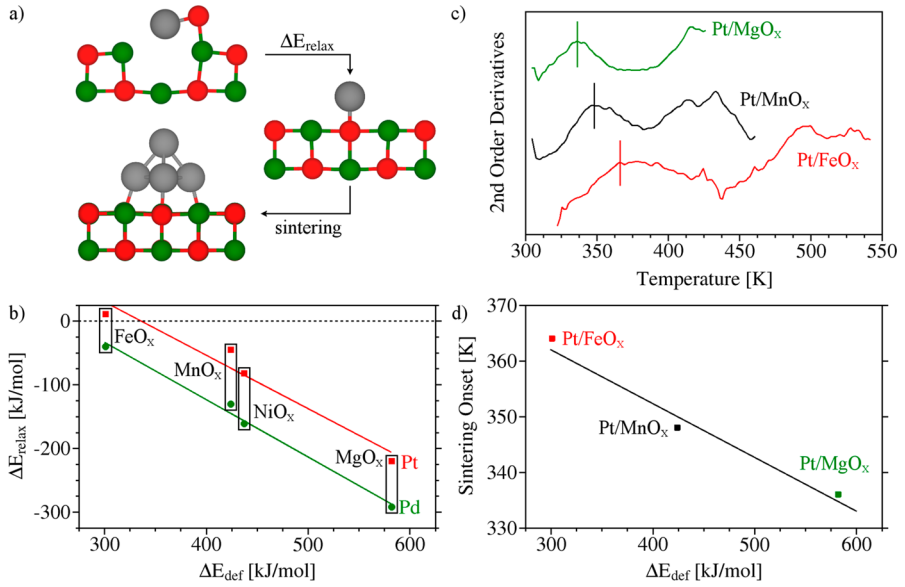

Figure 5. (a) Schematic representing the mechanism for catalyst deactivation upon healing the O vacancy and (b) reaction energies for the first deactivation step (ΔE_{relax}) as a function of the O vacancy formation energies (ΔE_{def}) for the single-atom catalysts considered in this work. (c) The experimentally measured onset temperature of Pt sintering is estimated from the maxima of the second order derivatives of the CO oxidation turnover frequencies (eq 6). (d) Sintering-onset temperatures determined from our experiments (panel c) decrease with increasing calculated O vacancy formation energies of the supporting oxide.

indicates that CO oxidation may also occur on the Pt clusters/particles, although less CO is converted there.

Furthermore, the H_2 uptake was measured for the Pt/MgO_x catalyst before and after the temperature-programmed CO oxidation experiments between 303 and 473 K. The H_2 uptake of the freshly prepared catalyst amounts to 0.13 μmol/g_{cat} after the pretreatment. After the temperature-programmed reaction (i.e., after the catalyst was exposed to CO and O_2 at 473 K), the H_2 uptake was below the uncertainty of our chemisorption experiments (<0.01 μmol/g_{cat}). For our 0.1 wt % Pt catalyst, this translates into a H/Pt ratio below 0.002, which is close to the value for extended Pt particles[59] and therefore indicates Pt sintering.

After Pt was deposited on the FeO_x support, a similar decrease in the amount of free O vacancy sites was observed via CO titration. On bare FeO_x, the total CO uptake amounts to 1.34 μmol/g_{cat}, which is significantly higher than on MgO_x due to the higher binding energy of CO (cf. Table S4). After Pt was added, the amount of weakly adsorbed CO decreased (0.95 μmol/g_{cat}), which indicates that Pt binds to the vacancies again. However, because of the mechanical properties of FeO, we were unable to prepare the pellets needed to perform infrared measurements. The hydrogen uptake of Pt/FeO_x prior to the temperature-programmed CO oxidation experiments (0.14 μmol/g_{cat}) is similar to the value for Pt/MgO_x (0.13 μmol/g_{cat}), indicating similar levels of Pt dispersion. After the CO oxidation experiments, the hydrogen uptake of Pt/FeO_x was lower (0.08 μmol/g_{cat}), but the decrease is significantly smaller than for Pt/MgO_x, which indicates lower sintering rates.

3.4. Catalyst Deactivation. For most supporting oxides considered in this work, DFT calculations show that the MeO species (**M3** in Figure 2) is metastable at the O vacancy, as the migration of the O atom (left behind after O_2 dissociation) into the vacancy (Figure 5a) is highly exothermic. The energy gain upon relaxation (ΔE_{relax}) depends on the O vacancy formation energy of the support, which is shown in Figure 5b for Pt and Pd on the four different supports considered here. For transition metal atoms supported on MgO(001), migration barriers obtained by Xu et al.[27] using DFT are below 80 kJ/mol. Since atomic dispersion is not favorable on the pristine (001) surfaces, metal particle formation (cf. Figure 5a) is predicted to occur readily even at moderate temperatures once the O vacancy is healed.

Temperature-programmed reaction experiments on Pt/FeO_x, Pt/MgO_x, and Pt/MnO_x show different temperature dependencies for CO oxidation rates at low and elevated temperatures. At low temperatures, turnover frequencies increase exponentially with 1/T, but as the temperature increases above a specific support-dependent temperature, the slope becomes steeper (i.e., the activation barrier increases), leading to turnover frequencies similar to metal particles.[60−62] The Arrhenius plots are shown in Figure S2. This behavior is attributed to catalyst sintering: as the Pt atoms begin to agglomerate, the identity of active site changes, leading to different CO oxidation barriers. Pt sintering was confirmed by H_2 chemisorption experiments as discussed in the previous section.

The onset temperature for Pt sintering was determined from our experiments by locating the inflection point of the temperature-dependent activation energy (i.e., the first derivative of ln(TOF) with respect to $1/T$), which is calculated using the finite difference approximation

$$\left.\frac{d[\ln \mathrm{TOF}]}{d[1000\mathrm{K}/T]}\right|_i \cong \frac{[\ln \mathrm{TOF}]_{i+1} - [\ln \mathrm{TOF}]_{i-1}}{[1000\mathrm{K}/T]_{i+1} - [1000\mathrm{K}/T]_{i-1}} \quad (6)$$

where TOF denotes turnover frequencies (per total number of Pt atoms) between 303 and 473 K and the subscript i denotes the corresponding indices of the data points. Noise was removed from this data using the moving average method with a period of 15. The second derivative, which has a maximum at the inflection point of eq 6, was then obtained using the same approach.

DOI: 10.1021/acscatal.8b03298
ACS Catal. 2019, 9, 1595−1604

Figure 5c shows the second-order derivatives of the rates, which have maxima at 336 K for Pt/MgO_x, 348 K for Pt/MnO_x, and 363 K for Pt/FeO_x. For Pd/MgO_x, Landman and co-workers[23] observed sintering around 300 K, which indicates that single Pd atoms are less stable than Pt atoms on O-defective MgO. This is in good agreement with our predictions from DFT: Pt atoms bind more strongly to O vacancies than Pd atoms (Figure 1), and ΔE_{relax} is less exothermic for Pt atoms (Figure 5b). Furthermore, sintering onset temperatures for Pt atoms determined in our experiments were found to decrease in the order FeO_x > MnO_x > MgO_x (Figure 5d) as predicted by ΔE_{def}. Therefore, transition metal atoms supported on metal oxides with high O vacancy formation energies are not suitable catalysts for reactions involving molecular oxygen, as metal particle formation is predicted to occur easily under reaction conditions.

In summary, the reducibility of the support is an important parameter for the stability of anionic single-atom catalysts. High O vacancy formation energies lead to strong binding of Pd and Pt atoms inside the vacancy, but the O vacancies heal quickly in an oxidizing environment, which leads to catalyst deactivation. On the other hand, support materials with low O vacancy formation energies bind Pd and Pt atoms less strongly. Therefore, metal oxides with intermediate O vacancy formation energies such as FeO and MnO are the most desirable support materials because they are able to stabilize transition metal atoms inside O vacancies that heal slowly in an oxidizing environment. Since CO oxidation barriers depend primarily on the identity of the transition metal atom (Table 2), changing the support does not affect the activity significantly.

4. CONCLUSIONS

On the basis of DFT calculations, we predict that Pd and Pt can form stable single-atom catalysts inside the O vacancies of MeO (Me = Fe, Mg, Mn, and Ni); for Pt/MgO_x, the presence of such species was confirmed using infrared spectroscopy. Metal atom binding energies inside the O vacancies depend on the vacancy formation energies of the supporting metal oxide and the lattice match between transition metal and support. Due to charge transfer into the metal d states, these systems can activate dioxygen at low temperatures by forming superoxide species; intrinsic barriers were found to depend primarily on the identity of the transition metal. On supporting metal oxides with O vacancy formation energies larger than FeO(001), the CO oxidation pathway involves a metastable metal monoxide species that can heal the O vacancy, leading to metal sintering and thus catalyst deactivation between 300 and 400 K. Therefore, the O vacancy formation energy of the support is an important parameter for the stability of anionic single-atom catalysts, while their activity depends primarily on the identity of the transition metal atom.

■ ASSOCIATED CONTENT

Supporting Information

The Supporting Information is available free of charge on the ACS Publications website at DOI: 10.1021/acscatal.8b03298.

Bulk metals; binding energies of transition metal atoms; descriptor for metal binding energies; binding energies and vibrational frequencies for adsorbed CO; barrier decomposition; Arrhenius plots and infrared spectra after CO oxidation; and structure files (PDF)

■ AUTHOR INFORMATION

Corresponding Authors

*E-mail: tekropp@wisc.edu.
*E-mail: emavrikakis@wisc.edu.

ORCID

Thomas Kropp: 0000-0002-9166-566X
Ya-Huei Cathy Chin: 0000-0003-4388-0389
Manos Mavrikakis: 0000-0002-5293-5356

Notes

The authors declare no competing financial interest.

■ ACKNOWLEDGMENTS

Work at UW−Madison has been supported by the U.S. Department of Energy (DOE) through the Office of Basic Energy Sciences (BES) by grant DE-FG02-05ER15731; work at the University of Toronto has been supported by the Natural Sciences and Engineering Research Council of Canada (NSERC). Computational work was performed using supercomputing resources at the UW−Madison Center for High Throughput Computing (CHTC), the Center for Nanoscale Materials (CNM) at Argonne National Laboratory under contract number DE-AC02-06CH11357, the Environmental Molecular Sciences Laboratory (EMSL) at Pacific Northwest National Laboratory (PNNL), and at the National Energy Research Scientific Computing Center (NERSC) under contract number DE-AC02-05CH11231. Thomas Kropp is grateful for partial financial support by the Alexander von Humboldt Foundation. We acknowledge Kyle Vollett and Haoyu Nie for carrying out the infrared spectroscopy studies.

■ REFERENCES

(1) Herzing, A. A.; Kiely, C. J.; Carley, A. F.; Landon, P.; Hutchings, G. J. Identification of active gold nanoclusters on iron oxide supports for CO oxidation. *Science* **2008**, *321*, 1331−1335.

(2) Vajda, S.; Pellin, M. J.; Greeley, J. P.; Marshall, C. L.; Curtiss, L. A.; Ballentine, G. A.; Elam, J. W.; Catillon-Mucherie, S.; Redfern, P. C.; Mehmood, F.; Zapol, P. Subnanometre platinum clusters as highly active and selective catalysts for the oxidative dehydrogenation of propane. *Nat. Mater.* **2009**, *8*, 213.

(3) Lei, Y.; Mehmood, F.; Lee, S.; Greeley, J.; Lee, B.; Seifert, S.; Winans, R. E.; Elam, J. W.; Meyer, R. J.; Redfern, P. C.; Teschner, D.; Schlögl, R.; Pellin, M. J.; Curtiss, L. A.; Vajda, S. Increased silver activity for direct propylene epoxidation via subnanometer size effects. *Science* **2010**, *328*, 224−228.

(4) Flytzani-Stephanopoulos, M.; Gates, B. C. Atomically dispersed supported metal catalysts. *Annu. Rev. Chem. Biomol. Eng.* **2012**, *3*, 545−574.

(5) Gates, B. C.; Flytzani-Stephanopoulos, M.; Dixon, D. A.; Katz, A. Atomically dispersed supported metal catalysts: perspectives and suggestions for future research. *Catal. Sci. Technol.* **2017**, *7*, 4259−4275.

(6) Liu, J. Catalysis by supported single metal atoms. *ACS Catal.* **2017**, *7*, 34−59.

(7) Hackett, S. F. J.; Brydson, R. M.; Gass, M. H.; Harvey, I.; Newman, A. D.; Wilson, K.; Lee, A. F. High-activity, single-site mesoporous Pd/Al_2O_3 catalysts for selective aerobic oxidation of allylic alcohols. *Angew. Chem., Int. Ed.* **2007**, *46*, 8593−8596.

(8) Moses-DeBusk, M.; Yoon, M.; Allard, L. F.; Mullins, D. R.; Wu, Z.; Yang, X.; Veith, G.; Stocks, G. M.; Narula, C. K. CO oxidation on supported single Pt atoms: Experimental and ab initio density functional studies of CO interaction with Pt atom on θ-Al_2O_3(010). *J. Am. Chem. Soc.* **2013**, *135*, 12634−12645.

(9) Narula, C. K.; Allard, L. F.; Stocks, G. M.; Moses-DeBusk, M. Remarkable NO oxidation on single supported platinum atoms. *Sci. Rep.* **2014**, *4*, 7238.

DOI: 10.1021/acscatal.8b03298
ACS Catal. 2019, 9, 1595−1604

(10) Peterson, E. J.; DeLaRiva, A. T.; Lin, S.; Johnson, R. S.; Guo, H.; Miller, J. T.; Hun Kwak, J.; Peden, C. H. F.; Kiefer, B.; Allard, L. F.; Ribeiro, F. H.; Datye, A. K. Low-temperature carbon monoxide oxidation catalysed by regenerable atomically dispersed palladium on alumina. *Nat. Commun.* **2014**, *5*, 4885.
(11) Zhang, Z.; Zhu, Y.; Asakura, H.; Zhang, B.; Zhang, J.; Zhou, M.; Han, Y.; Tanaka, T.; Wang, A.; Zhang, T.; Yan, N. Thermally stable single atom Pt/m-Al_2O_3 for selective hydrogenation and CO oxidation. *Nat. Commun.* **2017**, *8*, 16100.
(12) Bruix, A.; Lykhach, Y.; Matolínová, I.; Neitzel, A.; Skála, T.; Tsud, N.; Vorokhta, M.; Stetsovych, V.; Ševčíková, K.; Myslivečeka, J.; Fiala, R.; Václavů, M.; Prince, K. C.; Bruyère, S.; Potin, V.; Illas, F.; Matolín, V.; Libuda, J.; Neyman, K. M. Maximum noble-metal efficiency in catalytic materials: Atomically dispersed surface platinum. *Angew. Chem., Int. Ed.* **2014**, *53*, 10525−10530.
(13) Dvořák, F.; Farnesi Camellone, M.; Tovt, A.; Tran, N.-D.; Negreiros, F. R.; Vorokhta, M.; Skála, T.; Matolínová, I.; Myslivečeka, J.; Matolín, V.; Fabris, S. Creating single atom Pt-ceria catalysts by surface step decoration. *Nat. Commun.* **2016**, *7*, 10801.
(14) Nie, L.; Mei, D.; Xiong, H.; Peng, B.; Ren, Z.; Hernandez, X. I. P.; DeLaRiva, A.; Wang, M.; Engelhard, M. H.; Kovarik, L.; Datye, A. K.; Wang, Y. Activation of surface lattice oxygen in single-atom Pt/CeO_2 for low-temperature CO oxidation. *Science* **2017**, *358*, 1419−1423.
(15) Zhou, X.; Shen, Q.; Yuan, K.; Yang, W.; Chen, Q.; Geng, Z.; Zhang, J.; Shao, X.; Chen, W.; Xu, G.; Yang, X.; Wu, K. Unraveling charge state of supported Au single-atoms during CO oxidation. *J. Am. Chem. Soc.* **2018**, *140*, 554−557.
(16) Qiao, B.; Wang, A.; Yang, X.; Allard, L. F.; Jiang, Z.; Cui, Y.; Liu, J.; Li, J.; Zhang, T. Single-atom catalysis of CO oxidation using Pt_1/FeO_x. *Nat. Chem.* **2011**, *3*, 634.
(17) Lin, J.; Wang, A.; Qiao, B.; Liu, X.; Yang, X.; Wang, X.; Liang, J.; Li, J.; Liu, J.; Zhang, T. Remarkable performance of Ir_1/FeO_x single atom catalyst in water gas shift reaction. *J. Am. Chem. Soc.* **2013**, *135*, 15314−15317.
(18) Qiao, B.; Liang, J.-X.; Wang, A.; Xu, C.-Q.; Li, J.; Zhang, T.; Liu, J. J. Ultrastable single atom gold catalysts with strong covalent metal-support interaction (CMSI). *Nano Res.* **2015**, *8*, 2913−2924.
(19) Liang, J.; Yu, Q.; Yang, X.; Zhang, T.; Li, J. A systematic theoretical study on FeO_x-supported single atom catalysts: M_1/FeO_x for CO oxidation. *Nano Res.* **2018**, *11*, 1599−1611.
(20) Novotný, Z.; Argentero, G.; Wang, Z.; Schmid, M.; Diebold, U.; Parkinson, G. S. Ordered array of single adatoms with remarkable thermal stability: Au/Fe_3O_4(001). *Phys. Rev. Lett.* **2012**, *108*, 216103.
(21) Huang, Z.; Gu, X.; Cao, Q.; Hu, P.; Hao, J.; Li, J.; Tang, X. Catalytically active single atom sites fabricated from silver particles. *Angew. Chem., Int. Ed.* **2012**, *51*, 4198−4203.
(22) Abbet, S.; Riedo, E.; Brune, H.; Heiz, U.; Ferrari, A. M.; Giordano, L.; Pacchioni, G. Identification of defect sites on MgO(100) thin films by decoration with Pd atoms and studying CO adsorption properties. *J. Am. Chem. Soc.* **2001**, *123*, 6172−6178.
(23) Abbet, S.; Heiz, U.; Häkkinen, H.; Landman, U. CO oxidation on a single Pd atom supported on magnesia. *Phys. Rev. Lett.* **2001**, *86*, 5950−5953.
(24) Hoffman, A. S.; Debefve, L. M.; Zhang, S.; Perez-Aguilar, J. E.; Conley, E. T.; Justl, K. R.; Arslan, I.; Dixon, D. A.; Gates, B. C. Beating heterogeneity of single-site catalysts: MgO-supported iridium complexes. *ACS Catal.* **2018**, *8*, 3489−3498.
(25) Sanchez, A.; Abbet, S.; Heiz, U.; Schneider, W. D.; Häkkinen, H.; Barnett, R. N.; Landman, U. When gold is not noble: Nanoscale gold catalysts. *J. Phys. Chem. A* **1999**, *103*, 9573−9578.
(26) Yoon, B.; Häkkinen, H.; Landman, U.; Wörz, A. S.; Antonietti, J.-M.; Abbet, S.; Judai, K.; Heiz, U. Charging effects on bonding and catalyzed oxidation of CO on Au_8 clusters on MgO. *Science* **2005**, *307*, 403−407.
(27) Xu, H.; Xu, C.-Q.; Cheng, D.; Li, J. Identification of activity trends for CO oxidation on supported transition metal single atom catalysts. *Catal. Sci. Technol.* **2017**, *7*, 5860−5871.
(28) Kung, H. H.; Kung, M. C.; Costello, C. K. Supported Au catalysts for low temperature CO oxidation. *J. Catal.* **2003**, *216*, 425−432.
(29) Alayoglu, S.; Nilekar, A. U.; Mavrikakis, M.; Eichhorn, B. Ru−Pt core−shell nanoparticles for preferential oxidation of carbon monoxide in hydrogen. *Nat. Mater.* **2008**, *7*, 333.
(30) Liu, K.; Wang, A.; Zhang, T. Recent advances in preferential oxidation of CO reaction over platinum group metal catalysts. *ACS Catal.* **2012**, *2*, 1165−1178.
(31) Saavedra, J.; Doan, H. A.; Pursell, C. J.; Grabow, L. C.; Chandler, B. D. The critical role of water at the gold-titania interface in catalytic CO oxidation. *Science* **2014**, *345*, 1599.
(32) Blöchl, P. E. Projector augmented-wave method. *Phys. Rev. B: Condens. Matter Mater. Phys.* **1994**, *50*, 17953−17979.
(33) Kresse, G.; Joubert, D. From ultrasoft pseudopotentials to the projector augmented-wave method. *Phys. Rev. B: Condens. Matter Mater. Phys.* **1999**, *59*, 1758−1775.
(34) Kresse, G.; Furthmüller, J. Efficient iterative schemes for ab initio total-energy calculations using a plane-wave basis set. *Phys. Rev. B: Condens. Matter Mater. Phys.* **1996**, *54*, 11169−11186.
(35) Kresse, G.; Furthmüller, J. Efficiency of ab-initio total energy calculations for metals and semiconductors using a plane-wave basis set. *Comput. Mater. Sci.* **1996**, *6*, 15−50.
(36) Perdew, J. P.; Burke, K.; Ernzerhof, M. Generalized gradient approximation made simple. *Phys. Rev. Lett.* **1996**, *77*, 3865−3868.
(37) Anisimov, V. I.; Zaanen, J.; Andersen, O. K. Band theory and Mott insulators - Hubbard-U instead of Stoner-I. *Phys. Rev. B: Condens. Matter Mater. Phys.* **1991**, *44*, 943−954.
(38) Liechtenstein, A. I.; Anisimov, V. I.; Zaanen, J. Density functional theory and strong-interactions - orbital ordering in Mott-Hubbard insulators. *Phys. Rev. B: Condens. Matter Mater. Phys.* **1995**, *52*, R5467−R5470.
(39) Wang, L.; Maxisch, T.; Ceder, G. Oxidation energies of transition metal oxides within the GGA+U framework. *Phys. Rev. B: Condens. Matter Mater. Phys.* **2006**, *73*, 195107.
(40) Franchini, C.; Podloucky, R.; Paier, J.; Marsman, M.; Kresse, G. Ground-state properties of multivalent manganese oxides: density functional and hybrid density functional calculations. *Phys. Rev. B: Condens. Matter Mater. Phys.* **2007**, *75*, 195128.
(41) Rohrbach, A.; Hafner, J.; Kresse, G. Molecular adsorption on the surface of strongly correlated transition-metal oxides: A case study for CO/NiO(100). *Phys. Rev. B: Condens. Matter Mater. Phys.* **2004**, *69*, No. 075413.
(42) Dudarev, S. L.; Botton, G. A.; Savrasov, S. Y.; Humphreys, C. J.; Sutton, A. P. Electron-energy-loss spectra and the structural stability of nickel oxide: A LSDA+U study. *Phys. Rev. B: Condens. Matter Mater. Phys.* **1998**, *57*, 1505−1509.
(43) Henkelman, G.; Jónsson, H. A dimer method for finding saddle points on high dimensional potential surfaces using only first derivatives. *J. Chem. Phys.* **1999**, *111*, 7010−7022.
(44) Heyden, A.; Bell, A. T.; Keil, F. J. Efficient methods for finding transition states in chemical reactions: Comparison of improved dimer method and partitioned rational function optimization method. *J. Chem. Phys.* **2005**, *123*, 224101.
(45) Momma, K.; Izumi, F. VESTA 3 for three-dimensional visualization of crystal, volumetric and morphology data. *J. Appl. Crystallogr.* **2011**, *44*, 1272−1276.
(46) Richter, N. A.; Sicolo, S.; Levchenko, S. V.; Sauer, J.; Scheffler, M. Concentration of vacancies at metal oxide surfaces: Case study of MgO(100). *Phys. Rev. Lett.* **2013**, *111*, No. 045502.
(47) Pearson, W. B. *A Handbook of Lattice Spacings and Structures of Metals and Alloys*; Pergamon, 1958; Vol. *4*.
(48) O'Connor, N. J.; Jonayat, A. S. M.; Janik, M. J.; Senftle, T. P. Interaction trends between single metal atoms and oxide supports identified with density functional theory and statistical learning. *Nat. Catal.* **2018**, *1*, 531−539.
(49) Andersen, T.; Haugen, H. K.; Hotop, H. Binding energies in atomic negative ions III. *J. Phys. Chem. Ref. Data* **1999**, *28*, 1511−1533.

DOI: 10.1021/acscatal.8b03298
ACS Catal. 2019, 9, 1595−1604

(50) Pacchioni, G.; Freund, H.-J. Electron transfer at oxide surfaces. The MgO paradigm: From defects to ultrathin films. *Chem. Rev.* **2013**, *113*, 4035−4072.
(51) Jerratsch, J.-F.; Shao, X.; Nilius, N.; Freund, H.-J.; Popa, C.; Ganduglia-Pirovano, M. V.; Burow, A. M.; Sauer, J. Electron localization in defective ceria films: A study with scanning-tunneling microscopy and density-functional theory. *Phys. Rev. Lett.* **2011**, *106*, 246801.
(52) Del Vitto, A.; Pacchioni, G.; Delbecq, F.; Sautet. Sautet, P. Au atoms and dimers on the MgO(100) surface: A DFT study of nucleation at defects. *J. Phys. Chem. B* **2005**, *109*, 8040−8048.
(53) Hemmingson, S. L.; Campbell, C. T. Trends in adhesion energies of metal nanoparticles on oxide surfaces: Understanding support effects in catalysis and nanotechnology. *ACS Nano* **2017**, *11*, 1196−1203.
(54) Campbell, C. T.; Sellers, J. R. V. Anchored metal nanoparticles: Effects of support and size on their energy, sintering resistance and reactivity. *Faraday Discuss.* **2013**, *162*, 9−30.
(55) Lindstrom, P. J.; Mallard, W. G. *NIST Chemistry WebBook*; National Institute for Standards and Technology: Gaithersburg MD, 2018.
(56) Redhead, P. A. Thermal desorption of gases. *Vacuum* **1962**, *12*, 203−211.
(57) Wu, X.; Senapati, L.; Nayak, S. K.; Selloni, A.; Hajaligol, M. A density functional study of carbon monoxide adsorption on small cationic, neutral, and anionic gold clusters. *J. Chem. Phys.* **2002**, *117*, 4010−4015.
(58) Sicolo, S.; Sauer, J. Interaction of CO with electron-rich defects on MgO(100). *J. Phys. Chem. C* **2013**, *117*, 8365−8373.
(59) Wilson, G. R.; Hall, W. K. Studies of the hydrogen held by solids. XIX. H_2 and O_2 chemisorption on silica-supported platinum. *J. Catal.* **1972**, *24*, 306−314.
(60) Berlowitz, P. J.; Peden, C. H. F.; Goodman, D. W. Kinetics of carbon monoxide oxidation on single-crystal palladium, platinum, and iridium. *J. Phys. Chem.* **1988**, *92*, 5213−5221.
(61) Allian, A. D.; Takanabe, K.; Fujdala, K. L.; Hao, X.; Truex, T. J.; Cai, J.; Buda, C.; Neurock, M.; Iglesia, E. Chemisorption of CO and mechanism of CO oxidation on supported platinum nanoclusters. *J. Am. Chem. Soc.* **2011**, *133*, 4498−4517.
(62) Lachkov, P.; Chin, Y.-H. Catalytic consequences of reactive intermediates during CO oxidation on Ag clusters. *ACS Catal.* **2018**, *8*, 11987−11998.

DOI: 10.1021/acscatal.8b03298
ACS Catal. 2019, 9, 1595−1604